Unravelling the contribution of early postseismic deformation using sub-daily GNSS positioning

Cedric Twardzik[1*], Mathilde Vergnolle[1], Anthony Sladen[1], and Antonio Avallone[2]

[1]Université Côte d'Azur, CNRS, Observatoire de la Côte d'Azur, Geoazur, IRD, UMR 7329, 250 rue Albert Einstein, Sophia-Antipolis, 06560, Valbone, France.

[2]Istituto Nazionale di Geofisica e Vulcanologia, Osservatorio Nazionale Terremoti, Via di Vigna Murata 605, Rome, 00143, Italy.

[*]corresponding author: cedric.twardzik@geoazur.unice.fr

Abstract

After large earthquakes, some parts of the fault continue to slip for days to months during the afterslip phase. This behaviour has been documented for many earthquakes. Yet, little is known about the early stage, i.e., from minutes to hours after the mainshock. Its detailed study requires continuous high-rate position time series close to the fault, and advanced signal processing to accurately extract the surface displacements. Here, we use a refined kinematic precise point positioning processing to document the early postseismic deformation for three earthquakes along the South American subduction zone (2010 M_w8.8 Maule, Chile; 2015 M_w8.3 Illapel, Chile; 2016 M_w7.6 Pedernales, Ecuador). First, we show that the early postseismic signal can affect by more than 10% the estimates of coseismic offsets. This is because the early postseismic signal rises above the noise level as early as a few tens of minutes after the earthquake. Our analysis of the time series indicates that, over the first 36 hours, more than half of the deformation occurs within the first 12 hours, a time window often disregarded with daily positioning. This leads to significant errors on the total postseismic slip budget and the associated hazard on major faults.

(199/200 words)

Main text

Introduction

The postseismic phase marks the transition between the earthquake coseismic rupture and the interseismic phase, when the fault is re-locking. It was first documented in the early 1950's by Okuda (1950) and Okada and Nagata (1953), after the 1946 Nankaido, Japan earthquake (M_w8.1). In the mid- and late 1960's Tsubokawa et al. (1964) and Smith and Wyss (1968) made additional observations after the 1964, Niigita, Japan, earthquake (M_w7.6), and the 1966 Parkfield, California, earthquake (M_w6.0), respectively. With the advances of satellite geodesy in the 1990's, the number of observations has increased considerably, and the postseismic phase is now the focus of many studies (see for instance the data compilation from Ingleby and Wright 2017).

The term postseismic encompasses different processes occurring as a response of the earthquake rupture such as poroelastic and viscoelastic relaxation, or transient aseismic slip on the fault, called afterslip. In this study, we focus in particular on afterslip, which might hold some answers to several relevant questions about the physical properties of faults. First, the recovery of the spatial distribution of afterslip is a way to document the areas of the fault that might behave differently than the areas where the coseismic slip has occurred. Thus, it could help to constrain the level and scale of frictional heterogeneities, as well as the physical conditions driving slip on the fault. Afterslip also represents a large fraction of the total slip budget of a fault. Indeed, the amount of postseismic slip can sometimes exceed the coseismic slip after a few months or years. For instance, this is observed for the M_w7.7 1994 Sanriku-Haruka-Oki, Japan earthquake (Heki and Tamura 1997) or the M_w6.0 2004 Parkfield, California, earthquake (Freed 2007). We even observe that, for these two earthquakes, the equivalent moment magnitude of the early postseismic slip (i.e., after 5 days and 1 day, respectively), represents 30 and 50% of the coseismic moment magnitude (Heki and Tamura 1997, Langbein et al. 2005). Finally, many studies suggest that the afterslip might be a controlling mechanism of aftershocks as both phenomenon directly follow the mainshock and show a similar temporal evolution (e.g., Benioff 1951, Perfettini and Avouac 2004, Savage et al. 2007, Wennerberg and Sharp 1997).

Most postseismic studies model afterslip using rate-and-state friction, a formalism first introduced by Dieterich (1979), on the basis of observations from laboratory experiments. These studies show that the surface deformation induced by afterslip can be explained under this framework (e.g., Hsu et al. 2006, Johnson et al. 2006, Marone et al. 1991, Montesi 2004, Perfettini and Avouac 2004, Wennerberg and Sharp 1997). However, the onset of postseismic deformation (< 1 day) is critical to better understand the mechanics of afterslip. Wennerberg and Sharp (1997) have attempted to explain the surface observations after several earthquakes using the rate-and-state friction law, as well as the rate-dependent friction law, a widely used variant assuming steady-state. Even though both models are able to explain the surface observations, they show that when the models are extrapolated towards the origin time of the earthquake, the two start to diverge. This is also pointed out by Helmstetter and Shaw (2009), who have extended the comparison to the rate-and-state friction law under velocity-strengthening (i.e., stable aseismic slip) and velocity-weakening (i.e., unstable slip) regime, the rate-dependent friction law, and an empirical law based on the observed time decay of aftershocks. This discrepancy at the early stage of postseismic deformation have been explained by Perfettini and Ampuero (2008), based on a theoretical approach. They show that the response of a fault to a sudden stress perturbation follow two stages: (1) an initial acceleration of afterslip over a given time (t_{max}) up to a peak velocity, followed by (2) a long-term steady-state relaxation. Thus, the steady-state approximation that is generally used to model afterslip is only valid after a certain time (t_{max}). Perfettini and Ampuero (2008) have estimated that t_{max} ranges from 10^{-6} seconds up to 2 days. This latter result calls for more observations to precisely document what happens during the time frame from few seconds to few days after an earthquake. However, to date, only few observations on the onset of postseismic deformation, hereafter called early postseismic, are available.

Langbein et al. (2006) are among the first to investigate the early postseismic phase. They have used sub-daily GNSS position time series at 13 sites, with variable positioning intervals (1 minutes, 3 minutes, and 30 minutes) to capture the time evolution of the surface displacement after the 2004 Parkfield earthquake, as early as 100 seconds and up to 10 days after the mainshock. After that, they have used daily GNSS time series up to 9 months following the earthquake. They show that the entire time series at all sites can be explained by an Omori's-type friction law, as what is typically used to explain the behaviour of aftershocks (Omori 1894). Miyazaki and Larson (2008) went a step further by performing a spatiotemporal inversion of the afterslip after the 2003 Tokachi-Oki, Japan, earthquake ($M_w8.0$). They have used 30 seconds GNSS kinematic position time series that cover the first 4 hours following the mainshock. Their results show a complex pattern of afterslip on the fault. For the first hour, and preceding the occurrence of a large aftershock ($M_w7.4$), the afterslip reaches ∼3 cm of peak slip, and it is located in between the rupture area of the mainshock and that of the large aftershock. In the next three hours, a second patch of afterslip is observed. It has a larger peak slip (∼12 cm) and it is located down-dip of the rupture area of the mainshock. While it would be tempting to link the occurrence of the aftershock to the sudden change in behaviour of the time series, Fukuda et al. (2009) have been able to explain that change using the rate-and-state framework alone. This suggests that the acceleration phase predicted by Perfettini and Ampuero (2008) can be observed for this earthquake. Later, Malservisi et al. (2015) have looked at the early postseismic deformation (i.e., the first day) after the 2012 Nicoya, Costa Rica, earthquake (M_w7.6). They show that in this case, the postseismic deformation starts immediately after the mainshock, and decays very rapidly with time, since little displacement is observed beyond the first 3 hours. Thus, for this earthquake, the two phases of deformation are not observed. In addition, despite the fact that this earthquake has a smaller magnitude than the Tokachi-Oki earthquake, the inversion of the position time series shows that the peak slip amplitude of the early afterslip is about two times larger ($\sim$30 cm instead of $\sim$12 cm). Finally, on a similar time scale (4 hours), Munekane (2012) has looked at the 2011 Tohoku-Oki, Japan, earthquake (M_w9.1). Here, after 1 hour, the afterslip has reached a equivalent moment magnitude of 7.8, and a peak slip of $\sim$21 cm. Interestingly, this is about 30% less than for the Nicoya earthquake. Thus, early afterslip might not necessarily scale with the magnitude of the mainshock, as observed at the time scale of a few months (Lin et al. 2013).

The diversity of results regarding the early phase of the postseismic deformation, whether in terms of frictional properties, slip amplitude, or temporal evolution, stresses the need to better document this phase of the seismic cycle. As mentioned above, characterising the early afterslip is essential to understand how faults transition from coseismic fast slip to postseismic slow slip, both in space and time, and to refine its contribution to the total postseismic slip budget. In particular, considering that the amplitude of afterslip tends to decay exponentially with time, we can expect that the early postseismic deformation is significant. Thus, some fundamental questions are still pending such as how soon after an earthquake does start the afterslip ? Is the early postseismic deformation as significant as suggested by the exponential time decay ?

Because of the short time scale of the early postseismic deformation (few hours), we cannot use accurate daily GNSS position time series. Instead, if we want to observe the early stage of the postseismic deformation, we need to work on continuous sub-daily, high-frequency, GNSS position time series, but which in turn contain more noise. This requires the use of advanced kinematic processing and analysis techniques to isolate the emerging signal from the noise as early as possible. Here, we use a kinematic precise point positioning multi-stage strategy to process the 30-seconds continuous GNSS data, an adapted sidereal filtering to refine the position time series, and a statistical detection test to observe the early postseismic deformation following 3 megathrust earthquakes in South America: the 2010 Maule, Chile, earthquake (M_w8.8), the 2015 Illapel, Chile, earthquake (M_w8.3), and the 2016 Pedernales, Ecuador, earthquake (M_w7.6). Figure 1 shows the network of stations that we use for each earthquake. We have chosen these 3 earthquakes because of their relative proximity to the coast, maximising the chances to observed significant signal over the first few hours. With our processing and post-processing routines detailed in the Method Section, we obtain 30-seconds position time series over 10 days (6 days before the earthquake, the day of the earthquake itself, and 3 days after the earthquake) for 3-components and for a total of 53 stations. Hereafter, we only focus on the East component, which is the one that typically records the largest motion during and after large megathrust earthquakes on the South American subduction zone. Figures 1(ABC) show a sample of the time series that are representative of the data set that we are analysing in this study. We analyse these observations to evaluate how quickly we can detect surface displacement caused by the afterslip, and to document how intense is the early postseismic surface displacement. We then discuss the implication of our results on the estimation of the earthquake cycle slip budget.

(1517 words)

Results

A Early postseismic deformation greatly affect estimates of coseismic offsets

Our data processing strategy (see the Method Section) consists in processing separately the data before the earthquake (up to 30 seconds before the earthquake origin time) and after the earthquake (from 2.5 minutes after the earthquake). Thus, the coseismic offsets that we calculate from our time series are not affected by postseismic deformation. On the contrary, a significant number of studies use daily position time series to estimate the coseismic offsets, and the strategy used for the calculations varies across different studies. For instance, Lorito et al. (2011) use 7 to 8 days before the Maule earthquake to compute the pre-earthquake position and the position on the day of the earthquake to compute the post-earthquake position. Meanwhile, Ding et al. (2015) use 4 days before the earthquake and 4 days after the earthquake to compute the coseismic offsets of the 2013 Craig, Alaska, earthquake ($M_w7.5$). A similar approach is used by Nikolaishen et al. (2015) for the 2012, Haida Gwai, Canada, earthquake ($M_w7.8$), except that 7 days are used before and after the earthquake. Thus, it is clear that some postseismic deformation is included in these estimates.

Langbein et al. (2005) have attempted to quantify this effect for the 2004 Parkfield earthquake. They show that depending on the rate of positioning (1 minute, 30 minutes, 1 day), the estimated coseismic offsets can differ by a few millimetres. Hill et al. (2012) have done a similar study after the 2012 Mentawai, Indonesia, earthquake ($M_w7.8$). They have compared the coseismic offsets estimated from daily position time series and those estimated from 1-seconds position time series. For the former, they use 8 days before and after the earthquake, while 90 seconds of data on either side of the earthquake are used for the latter, with the 2-minutes following the earthquake origin time being avoided. They show that the coseismic offsets using the 1-seconds position time series are smaller than the estimates from daily positions time series. In fact, they estimate that 30% of the offsets measured from daily position time series is not caused by the earthquake but by afterslip.

Here, we further quantify the bias from including postseismic deformation into the estimates of coseismic offsets. To do that, we compare the strict coseismic offsets calculated from the 30-seconds position time series, with offsets determined by averaging the position time series over one, two and three days before and after the earthquake. We find that the difference between the strict coseismic offsets and those estimated using averages over one or several days is ∼34% (see Figure 2). This is consistent with what has been determined by Hill et al. (2012) for the Mentawai earthquake. As expected, we observe that when the offsets are large (> 50 cm), the contribution of early postseismic deformation is small (<10%). On the contrary, Figure 2 shows that care must be taken when dealing with small coseismic offsets since the impact of early postseismic deformation could be significant (up to 200%).

(469 words)

B Postseismic deformation can be observed within tens of minutes after an earthquake

Before analysing the amount of deformation that is observed during the early stage of the postseismic phase, it is important to define how early we can start to observe it. This is a major question since, prior to the detection of this onset time, we cannot distinguish between a model where the afterslip is almost zero and one where the afterslip has started but its amplitude is not yet large enough to generate a detectable signal at the surface.

To address this question, we apply an algorithm that aims to detect a significant change of the mean for a given time series. Effectively, we search for the time when the mean of the time series changes by more than 3 times the standard deviation of the time series, the latter being determined using the 6 days of observations before the earthquake. In addition, this change of mean must be sustained over more than 70% of the time period that follows the detection time (see the Methods Section for more details). Hence, the detection of the onset time of the postseismic deformation is controlled both by the noise level of the time series as well as the intensity of the postseismic deformation.

Figure 3 and Table 1 summarises the results. First, we observe that the onset of the postseismic displacement is detected for ∼43% of the time series (i.e., 23 over 53 stations). This represents a significant percentage of detection considering that some stations are located far from the epicentres of the earthquakes (up to 250 km from the centroid). For 78% of the successful detections, the postseismic signal rises above the noise level within the first 2 hours. In fact, for large postseismic displacements (i.e., more than 3 cm measured at 12 hours), we always detect its onset within the first 2 hours, regardless of the noise level of the time series, the latter ranging from 3 to 7 mm. We also observe that several stations exhibit a significant signal as early as ∼10 minutes after the earthquake origin time, suggesting a very rapid deformation. On the other hand, when the postseismic signal has a smaller amplitde (< 3 cm at 12 hours), the onset time spreads over a larger range (i.e., from few minutes to 10 hours). In addition, we observe that if less than ± 2 cm is measured after 12 hours, we cannot detect the onset of the postseismic deformation. These results suggest that the detection of the onset time is essentially controlled by the amplitude of the postseismic displacement.

In summary, we observe that at some stations, the postseismic signal can rise above the noise level as early as ∼10 minutes after the earthquake, and mainly within the first 2 hours. The next step is to quantify the contribution of the early stage of the postseismic phase (i.e., the first few hours), with respect to what is traditionally observed using daily position time series.

(484 words)

C Daily positioning is blind to a large fraction of the postseismic deformation

Using daily positioning, i.e., when the 24 hours of recorded data are reduced to a daily position, the effective time of the positioning is based on a weighted average of the available data. Assuming that the record does not contain gaps, the effective time of the position corresponds to the middle of the time window used to determine that position. As daily positioning strategy usually uses 24 hours blocks of data, the first point of the postseismic time series is on the day after the earthquake. Thus, with respect to the origin time of the earthquakes considered in this study – 06:34:12 UTC, 22:54:33 UTC, and 23:58:37 UTC for the Maule, Illapel, and Pedernales earthquakes, respectively – the effective time of the first daily position is going to be 29.4 hours, 13.1 hours and 12.0 hours after the origin time of these earthquakes. In some cases, if there are enough data available between the earthquake origin time and the end of the day (23:59:59 UTC), a position can be obtained on the day of the earthquake. For instance, for the Maule earthquake, it is possible to use the data from 06:34:12 UTC to 23:59:59 UTC to obtain a position on the day of the earthquake. In that case, the postseismic position time series will start ∼9 hours after the earthquake origin time.

Consequently, the daily positioning strategy usually implies that a few hours of postseismic deformation are not included into the overall postseismic deformation budget, despite being a time period when the slip-rate is supposed to be the large (see Figure 4). However, with high-rate kinematic position time series, we can quantify the amount of early postseismic deformation that is usually not included in daily position time series. Because the time between the origin time of the earthquake and the first daily position varies from one earthquake to another, we are going to assume a standard case in which the first daily position comes 12 hours after the mainshock. This is equivalent to a case where the earthquake occurs close to 23:59:59 UTC and it allows us to make conservative estimates with respect to the different possible scenarios.

First, we select 3 windows that are 30 minutes long and centred at 30 minutes, 12 hours, and 36 hours after the earthquake origin time. For each window, we compute the average position. The difference between the position at 12 hours and that at 36 hours reproduces the traditional postseismic observation that can be made using daily positioning. On the other hand, the difference between the position at 30 minutes and that at 12 hours represents the amount of deformation that can only be observed using sub-daily positioning (see Figure 4). Note that we are aware that we only approximate the real case. Since daily positioning techniques use data over 24 hours, the obtained position do not actually stand on the kinematic position time series. Instead, it is above (or below), and the more the rate of deformation is important, the more the shift gets large. It will tend towards the kinematic position time series as the rate of deformation becomes smaller and smaller. Thus, we slightly overestimate the difference compared to the real case.

Figure 5 summarises the results for all the stations for which the onset time of the postseismic deformation could be detected (see the previous Section). It shows that most of the displacement occurs within the first 12 hours. On average, for the East component, we find that ∼64% of the displacement that is measured over 36 hours is in fact occuring during the first 12 hours. To the first order, this is consistent with a logarithmic decay of the postseismic surface deformation with a relaxation time of about 3.0 hours ($\frac{\log(1+12h/3h)}{\log(1+36h/3h)} \sim 63\%$). Thus, it clearly highlights the fact that a significant amount of surface deformation occurs very early after the earthquake, and it is not accounted for when daily positioning is used to study the postseismic deformation.

(667 words)

Discussion and conclusive remarks

In this study, we provide a detailed analysis on the emergence of postseismic surface displacement signal in high-rate kinematic position time series for three subduction zone earthquakes. While three more earthquakes might not seem like a significant increase, it nearly doubles the number of observations about the early stage of the postseismic phase.

First, our results indicate that the use of daily solutions to estimate the coseismic offsets introduces an average error of ∼34%. That error depends on the amplitude of the offsets : (1) for offsets more than 50 cm, using daily positions leads to less than 10% of error, while (2) for offsets smaller than 50 cm, the error can be large (from ∼0 to 200%). These estimates have important implications for the studies of the earthquake rupture, especially those using geodetic data. In particular, they can be used to estimate the error made on coseismic rupture model from InSAR and/or GNSS data.

Regarding the postseismic deformation itself, we observe that most of the examples available to us, meaning this study as well as those of Langbein et al. (2005), Munekane (2012) and Malservisi et al. (2015), show an almost immediate and intense start of the postseismic surface deformation. Thus, the observations for the Tokachi-Oki earthquake, which show an early postseismic signal that behaves in two phases (Miyazaki and Larson 2008) appears to be an exception. Interestingly, this 2-phases behavior is predicted by the rate-and-state framework (e.g., Perfettini and Ampuero 2008 and Fukuda et al. 2009). However, as pointed out by Perfettini and Ampuero (2008), the time scale of the acceleration phase ranges from 10^{-6} seconds up to 2 days. Thus, it is possible that, for most cases, this initial accelaration phase is too short to be observed. It is also possible that, for most of the cases, the behavior of early postseismic deformation might simply be rate-dependent.

Even if the acceleration phase lasts a long enough time, it needs to produce enough surface displacement to rise above the noise level of the time series and thus be observable. Following our detection technique, this would mean that the afterslip during the acceleration phase should produce a surface displacement that is about 3.3 times the noise level of the time series. Since the average noise level over all of our time series is ∼5 mm, it means that afterslip should generate more than 1.5 cm of surface deformation. To assess how this translates in term of slip on the fault, we have perform a set of forward calculations (see Figure 6). For each earthquake we create a distribution of dislocations of 20 km^2, consistent with the geometry of the slab. For each dislocation, we search for the equivalent moment magnitude (M_{eq}) that generates more than 1.5 cm of surface displacement on the East component for at least one station of the network. We find that for the Maule and Illapel earthquakes, the network is able to detect afterslip if M_{eq} is larger than 8.0. The network in Ecuador, thanks to its density and its proximity to the trench, is able to detect afterslip at a lower magnitude (M_{eq} ∼7.7). This is consistent with the results of Miyazaki and Larson (2008) for the Tokachi-Oki earthquake. Indeed, they find an acceleration phase that lasts about one hour and that reaches a magnitude of ∼7.2 (this is estimated using Figure 3c of Miyazaki and Larson 2008, assuming a rupture area of 9.0×10^3 km^2, a peak slip of 3.0 cm and a rigidity of 30 GPa).

In any case, the fact that we can detect postseismic signal as early as a few tens of minutes after the earthquake origin time advocates for the use of kinematic processing strategy to study the postseismic deformation as early as possible after the mainshock. It suggests that we could get some early indications about the areas that are experiencing afterslip, which could have important implications regarding the assessement of areas of future large aftershocks. In their analysis of the 1992 Landers, California, earthquake (M_w7.2), Perfettine and

Avouac (2007) show that the aftershocks and the afterslip follow the same temporal evolution and are related in space to the stress changes induced by the progression of afterslip. More detailed studies are still needed, but it alludes to the possibility of using fast detection of early postseismic deformation to anticipate the areas that will host future aftershocks. This is even more critical since we know from the Omori's law that the rate of aftershocks will decrease by 2 to 3 order of magnitude after just one day (e.g., Enescu et al. 2009 on moderate-size earthquakes or Lengliné et al. 2012 on the 2011 Tohoku-Oki earthquake).

Regarding the intensity of early postseismic deformation, our results show that the cumulative deformation over the first 36 hours is essentially occurring during the first 12 hours, a timeframe that is not fully accessible using daily positioning. Thus, it is going to affect the slip budget of afterslip (several millimetres compared to few centimetres of surface displacements). For instance Klein et al. (2016), using daily position time series, have studied five years of postseismic deformation following the 2010 Maule earthquake. For two stations (CONZ and MAUL), they observe 40 cm and 70 cm of cumulative East displacement over 5 years (Figure 1 and 11 of Klein et al. 2016). As mentioned before, the use of daily positions makes that the first point of their postseismic time series is on the day after the earthquake, i.e., about 30 hours of early postseismic displacement is missing. We have calculated that over this time period, $\sim$9.6 cm and $\sim$6.4 cm are measured on CONZ and MAUL, respectively, corresponding to about 25% and about 10% of additional surface displacement. We reach a similar conclusion in the case of the 2016 Pedernales earthquake. Using daily positioning over a time period of 30 days, Rolandone et al. (2018) observe about 6.5 cm, 10.5 cm and 12.0 cm of cumulative East displacement for the stations PDNS, CABP and MOMP, respectively. In their study, the effective origin time of the postseismic time series is 12 hours after the earthquake. During the first 12 hours, we measure 1.7 cm, 2.2 cm and 1.7 cm of cumulative East displacement for the stations PDNS, CABP and MOMP, respectively, which corresponds to about 26%, 21% and 14% of additional surface displacement. These two examples show that the analysis of afterslip, when based on daily positioning only can strongly underestimate the amount of afterslip on the fault.

To conclude, the current processing strategy of continuous high-rate GNSS data allows to better resolve the temporal resolution of afterslip, in particular at the time scale of the first few hours. We can now access the full surface displacement history at a given station from the fist minutes after the earthquake, and up to several years. The accurate observations of the early postseismic stage is set to provide an enriched picture of the overall postseismic process and to shade light on the underlying physics. And, as we get closer in time to the mainshock, we can start to better document the transition from fast coseismic slip to slow postseismic slip.

(1132 words)

(4269/4500 words)

Methods

A Kinematic precise point positioning strategy

The high-rate position time series are obtained using the GD2P module of GIPSY-OASIS 6.4 software (Lichten and Border 1987) that is developed by the Jet Propulsion Laboratory (JPL). Our processing strategy is similar to that of Miyazaki and Larson (2008) and Malservisi et al. (2015). We use the precise point positioning strategy of Zumberger et al. (1997) including the phase ambiguity resolution from a single receiver (Bertiger et al. 2010). We use the final orbits and satellite clock estimates provided by the JPL. We account for ocean loading effects using the FES2004 model (Lyard et al. 2006). The tropospheric delays are calculated using the VMF1 mapping functions (Boehm et al. 2006). We account for higher order ionospheric terms using the IRI-2012b model (Bilitza et al. 2014). We set the input parameters as suggested by the GIPSY-OASIS documentation except for two parameters. We use 9.0×10^{-8} km/$\sqrt{s}$ for the troposphere zenith random walk parameter as suggested by Selle and Desai (2016) and 3.0×10^{-7} km/$\sqrt{s}$ for the random walk parameter of the Kalman filter for the kinematic positioning according to Choi (2007).

We process 6 days before the earthquake, the day of the earthquake, as well as 3 days after the earthquakes. The six days before the earthquake are used to build the sidereal filter (see the next section). For each UTC day, we follow the flowchart described in Appendix A. First, the data are processed using a static strategy to estimate the tropospheric delays and gradients (Step 1). These delays and gradients are used for the kinematic processing (Step 2). The obtained 30-seconds kinematic position time series is used for a new run with a static strategy, which refines the estimates of the tropospheric delays and gradients (Step 3). Once again, the estimated delays and gradients are used to perform a new kinematic processing (Step 4). A final kinematic processing is performed (Step 5), which uses the obtained 30-seconds kinematic position time series from the previous Step.

As the maximum expected displacement from one epoch to another is directly dependent in the tuning of the random walk epoch-by-epoch position estimation, we prefer to remove the coseismic part in the observations, which produces larger dynamic displacement than the postseismic ones. Thus, for the day of the earthquake, the RINEX file is cut into two pieces. The pre-earthquake file stops 30 seconds before the earthquake origin time, and the post-earthquake file starts 2.5 minutes after the earthquake origin time. Each step described above are performed for each piece independently, except for Step 3. For this Step, we estimate the tropospheric delays and gradients using the full RINEX file, and using the two kinematic position time series from Step 2, merged together. This is to avoid any discontinuity in the troposphere parameter estimation.

To minimise the discontinuities at the UTC day transition, we process 30-hours long RINEX file (i.e., from 21:00:00 UTC of day minus one to 03:00:00 UTC of day plus one). Thus, each position time series overlap with the next one over a six hours time window. We merge successive time series by choosing the point within the overlapping time window when the difference between the two time series is minimum.

The quality of the strategy is quantified using the reduction of the postfit residuals for the LC phase combination for each step of the processing. The average LC residuals for the static runs (Step 1 and 3) are 9.9×10^{-6} km and 8.8×10^{-6} km. Thus, using a-priori position time series rather than a constant a-priori position leads to a 10% reduction of the phase residuals. For the kinematic runs (Step 2, 4 and 5), we get 9.1×10^{-6} km, 9.0×10^{-6} km, and 8.8×10^{-6} km, meaning that the multi-step strategy leads to an overall 3% reduction of the phase residuals.

(597 words)

B Sidereal filtering

First, we use the 6 days before the earthquake to estimate a linear trend that is removed from the entire time series. Then, we attempt to minimuse the effects of multipaths and other kinds of perturbations caused by the geometry of the satellites by applying a sidereal filter to the time series (Nikolaidis et al. 2001 and Choi et al. 2004).

Choi et al. (2004) have shown that the sidereal period is not the same for all satellites. Thus, they suggest to keep the same set of satellites over the entire time period that is processed to ensure that the estimated sidereal period is appropriate at all times. This approach has the disadvantage of reducing the number of satellite used to obtain the position time series. In addition, the traditional sidereal filter relies on the use of a ∼24 hours window to filter the next ∼24 hours window, and so on. Thus, if the time series exhibits a significant trend over a long time, as we might expect for the postseismic deformation, the filtering might introduce spurious effects. To overcome this issue, we adopt a different approach, and use a sidereal filter that is based on cross-correlating successive days (e.g., Ragheb et al. 2007). The idea is to constructively stack the repeating patterns over several days, only on days when no earthquakes or postseismic trend is observed, i.e., on the 6 days before the earthquake. Because the sidereal filter is built over 6 days, we believe that it is representative of the sidereal signature of the site over the whole time period that we want to filter, eliminating the need of a constant satellite constellation through time. In addition, we can filter the postseismic time period without introducing artefacts that might arise because of the significant postseismic trend, which we do not want to remove.

In practice, we cross-correlate the first two days to determine the time lag that maximises the cross-correlation. Then, we shift and stack these two days to produce the first version of the sidereal filter. After that, we cross-correlate the sidereal filter with the third day. Again, we shift and stack the third day with the sidereal filter based on the cross-correlation. This process is repeated for the 6 days that precede the mainshock. Once built, we remove the mean and the linear trend of the sidereal filter. Then, we cross-correlate the sidereal filter with each day of the full time series and the sidereal filter is then removed from the time series (see Figure 7). To ensure that we are not introducing spurious effects, we only apply the filter if, during its construction, the average cross-correlation between the different days and the sidereal filter is above 0.3. The different figures in Appendix B summarises the effectiveness of the filter by showing the reduction of the standard deviation of the time series after applying the sidereal filter. It shows that the standard deviation of the time series goes on average from 6.8 mm to 4.8 mm on the North component, from 7.1 to 5.0 mm on the East component and from 13.5 to 10.0 mm on the Vertical component.

(505 words)

C Detecting the onset time of postseismic displacement

To detect the onset time of the postseismic displacement, we design an algorithm to estimate when the mean of the position time series changes significantly and remains at its new level. For that, we assume that the position time series follows a normal distribution. The algorithm for the detection is based on the Chow-test (Chow 1960), which tests the significance of using two linear regression to model a given dataset.

The null hypothesis assumes that the time series do not exhibit a change of mean. Thus the residual sum of squares for the null hypothesis is :

$$S_0 = \sum_{i=1}^{N} (u_i - \bar{u})^2 \tag{1}$$

where u_i is the position at time i, and $\bar{u}$ is the mean of the time series over N points. The alternative hypothesis is that there is a change of mean of the time series at a given breakpoint τ. Similarly, we can compute the residual sum of squares for the two sets:

$$S_{12} = S_1 + S_2 = \sum_{i=1}^{\tau} (u_i - \bar{u})^2 + \sum_{j=\tau+1}^{N} (u_j - \bar{u})^2 \tag{2}$$

Once we have computed this two quantities, we can compute the Chow-test statistic that is:

$$\chi = \frac{(S_0 - S12)/k}{S_{12}/(N_1 + N_2 - 2k)} \tag{3}$$

where N_1 and N_2 are the number of observations in each group and k is the number of parameters (in this case $k = 1$).

In practice, we slide a 12-hours long window (i.e., 1440 points), over the entire time series with a step of 30 seconds. At each step, we compute χ assuming that the potential breakpoint is at the centre of the window (i.e., $\tau = 720$ points and $N_1 = N_2 = 720$ points). Like this, we test every point as a potential breakpoint. Then, several criterion are applied to determine the point when we start to observe significant postseismic deformation.

First, we identify all the peaks in the χ time series that are above 3.3 times its own standard deviation, giving us a set of potential time for the breakpoint. Then, we only consider those that are after the earthquake origin time. Finally, we go through all of them and, for each, we test whether at least 70% of the time series after the peak has a mean that differs from the pre-seismic mean by at least 3.3 times the RMS of the time series. We set the onset time of the postseismic deformation to be the first one in time that successfully pass all the criterion. Figure 8 illustrates this method for a given time series.

(362 words)

(1464/1500 words)

References

H. Benioff. Earthquakes and rock creep (Part I: Creep and characteristics of rocks and the origin of aftershocks). *Bull. Seism. Soc. Am.*, 41(1):31–62, 1951.

W. Bertiger, S. D. Desai, B. Haines, N. Harvey, A. W. Moore, S. Owen, and J. P. Weiss. Single receiver phase ambiguity resolution with GPS data. *J. Geod.*, 84(5):327–337, 2010.

D. Bilitza, D. Altadill, Y. Zhang, C. Mertens, V. Truhlik, P. Richards, L.-A. McKinnell, and B. Reinisch. The international reference ionosphere 2012 - A model of internation collaboration. *J. Space Weather Space Clim.*, 4:A07, 2014.

J. Boehm, A. Niell, P. Tregoning, and H. Schuh. Global Mapping Function (GMF): A new empirical mapping function based on numerical weather model data. *Geophys. Res. Lett.*, 33:L07304, 2006.

K. Choi. Improvements in GPS precision: 10-Hz to one day. *Doctoral Dissertation, University of Colorado*, 2007.

K. Choi, A. Bilich, K. M. Larson, and P. Axelrad. Modified sidereal filtering: Implications for high-rate GPS positioning. *Geophys. Res. Lett.*, 31:L22608, 2004.

G. C. Chow. Tests of equality between sets of coefficients in two linear regressions. *Econometrica*, 29:591–605, 1960.

J. H. Dieterich. Modeling of rock friction: 1. Experimental results and constitutive equations. *J. Geophys. Res.*, 84(B5):2161–2168, 1979.

K. Ding, J. T. Freymueller, Q. Wang, and R. Zou. Coseismic and early postseismic deformation of the 5 January 2013 M_w7.5 Craig earthquake from static and kinematic GPS solutions. *Bull. Seis. Soc. Am.*, 105 (2B):1153–1164, 2015.

B. Enescu, J. Mori, M. Miyazawa, and Y. Kano. Omori-Utsu law c-values associated with recent moderate earthquakes in Japan. *Bull. Seism. Soc. Am.*, 99(2A):884–891, 2009.

A. M. Freed. Afterslip (and only afterslip) following the 2004 Parkfield, California, earthquake. *Geophys. Res. Lett.*, 34:L06312, 2007.

J. Fukuda, K. M. Johnson, K. M. Larson, and S. Miyazaki. Fault friction parameters inferred from the early stages of afterslip following the 2003 Tokachi-Oki earthquake. *J. Geophys. Res.*, 114:B04412, 2009.

K. Heki and Y. Tamura. Silent fault slip following an interplate thrust earthquake at the Japan trench. *Nature*, 386:3285–3288, 1997.

A. Helmstetter and B. E. Shaw. Afterslip and aftershocks in the rate-and-state friction law. *J. Geophys. Res.*, 114:B01308, 2009.

E. M. Hill, J. C. Borrero, Z. Huang, Q. Qiu, P. Banerjee, D. H. Natawidjaja, P. Elosegui, H. M. Fritz, B. W. Suwargadi, I. R. Pranantyo, L. Li, K. A. Macpherson, V. Skanavis, C. E. Synolakis, and K. Sieh. The 2010 M_w7.8 Mentawai earthquake: Very shallow source of rare tsunami earthquake determined from tsunami field survey and near-field GPS data. *J. Geophys. Res.*, 117:B06402, 2012.

Y.-J. Hsu, M. Simons, J. P. Avouac, J. Galetzka, K. Sieh, M. Chlieh, D. Natawidjaja, L. Prawirodirdjo, and Y. Bock. Frictional afterslip following the 2005 Nias-Simeulue earthquake, Sumatra. *Science*, 312(B5):1921–1926, 2006.

T. Ingleby and T. Wright. Omori-like decay of postseismic velocities following continental earthquakes. *Geophys. Res. Lett.*, 44:3119–3130, 2017.

K. M. Johnson, R. Bürgmann, and K. Larson. Frictional properties on the San Andreas fault near Parkfield, California, inferred from models of afterslip following the 2004 earthquake. *Bull. Seism. Soc. Am.*, 96(4B): S321–S338, 2006.

E. Klein, L. Fleitout, C. Vigny, and J. D. Garaud. Afterslip and viscoelastic relaxation model inferred from the large-scale post-seismic deformation following the 2010 M_w8.8 Maule earthquake (Chile). *Geophys. J. Int.*, 205:1455–1472, 2016.

J. Langbein, R. Borcherdt, D. Dreger, J. Fletcher, J. L. Hardebeck, M. Hellweg, C. Ji, M. Johnston, J. R. Murray, R. Nadeau, M. J. Rymer, and J. A. Treiman. Preliminary report on the 28 September 2004 M6.0 Parkfield, California, earthquake. *Seism. Res. Lett.*, 76(1):10–26, 2005.

J. Langbein, J. R. Murray, and H. A. Snyder. Coseismic and initial postseismic deformation from the 2004 Parkfield, California, earthquake, observed by Global Positioning System, electronic distance meter, creepmeters, and borehole strainmeters. *Bull. Seism. Soc. Am.*, 96(4B):S304–S320, 2006.

O. Lengliné, B. Enescu, Z. Peng, and K. Shiomi. Decay and expansion of the early aftershock activity following the 2011 M_w9.0 Tohoku, earthquake. *Geophys. Res. Lett.*, 39:L18309, 2012.

S. M. Lichten and J. S. Border. Strategies for high-precision Global Positioning System orbit determination. *Geophys. Res. Lett.*, 92(B12):12751–12762, 1987.

Y.-N. N. Lin, A. Sladen, F. Ortega-Culaciati, M. Simons, J. P. Avouac, E. J. Fielding, B. A. Brooks, M. Bevis, J. Genrich, A. Rietbrock, C. Vigny, R. Smalley, and A. Socquet. Coseismic and postseismic slip associated with the 2010 Maule earthquake, Chile: Characterising the Arauco Peninsula barrier effect. *J. Geophys. Res.: Solid Earth*, 118:3142–3159, 2013.

S. Lorito, F. Romano, S. Atzori, X. Tong, A. Avallone, J. McCloskey, M. Cocco, E. Boschi, and A. Pianatesi. Limited overlap between the seismic gap and coseismic slip of the great 2010 Chile earthquake. *Nat. Geo.*, 4: 173–177, 2011.

F. Lyard, F. Lefevre, T. Letellier, and O. Francis. Modelling the global ocean tides: Modern insight from FES2004. *Ocean Dyn.*, 56(5-6):394–415, 2006.

R. Malservisi, S. Y. Schwartz, N. Voss, M. Protti, V. Gonzalez, T. H. Dixon, Y. Jiang, A. V. Newman, J. Richardson, J. I. Walter, and D. Voyenko. Multiscale postseismic behavior on a megathrust: The 2012 Nicoya earthquake, Costa Rica. *Geochem. Geophys. Geosyst.*, 16:1848–1864, 2015.

L. Manshina and D. E. Smylie. The displacement fields of inclined faults. *Bull. Seism. Soc. Am.*, 61(5): 1433–1440, 1971.

C. J. Marone, C. H. Scholtz, and R. Bilham. On the mechanics of earthquake afterslip. *J. Geophys. Res.*, 96 (B5):8441–8452, 1991.

S. Miyazaki and K. Larson. Coseismic and early postseismic slip for the 2003 Tokachi-Oki earthquake sequence inferred from GPS data. *Geophys. Res. Lett.*, 35:L04302, 2008.

L. G. J. Montesi. Controls of shear zone rheology and tectonic loading on postseismic creep. *J. Geophys. Res.*, 109:B10404, 2004.

H. Munekane. Coseismic and early postseismic slips associated with the 2011 off the Pacific coast of Tohoku earthquake sequence: EOF analysis of GPS kinematic time series. *Earth Planets Space*, 64:1077–1091, 2012.

R. M. Nikolaidis, Y. Bock, P. J. de Jonge, D. C. Agnew, and M. Van Domselaar. Seismic wave observations with the Global Positioning System. *J. Geophys. Res.*, 106(B10):21897–21916, 2001.

L. Nikolaishen, H. Dragert, K. Wang, T. James, and H. Schmidt. Gps observations of crustal deformation associated with the 2012 M_w7.8 Haida Gwai earthquake. *Bull. Seism. Soc. Am.*, 105:1241–1252, 2015.

J.-M. Nocquet, P. Jarrin, M. Vallée, P. A. Mothes, R. Grandin, F. Rolandone, B. Delouis, H. Yepes, Y. Font, D. Fuentes, M. Régnier, A. Laurendeau, D. Cisneros, S. Hernandez, A. Sladen, J.-C. Singaucho, H. Mora, J. Gomez, L. Montes, and P. Charvis. Supercycle at the Ecuadorian subduction zone revealed after the 2016 Pedernales earthquake. *Nat. Geo.*, 10:145–149, 2016.

A. Okada and T. Nagata. Land deformation of the neighbourhood of Muroto Point after the Nankaido great earthquake in 1946. *Bull. Earthq. Res. Inst.*, 32:167–177, 1953.

T. Okuda. On the mode of the vertical land deformation accompanying the great Nankaido earthquake. *Bull. Geogr. Surv. Inst.*, 2(1):37–59, 1950.

F. Omori. On after-shocks. *Seism. J. Japan*, 19:71–80, 1894.

H. Perfettine and J.-P. Avouac. Modeling afterslip and aftershocks following the 1992 Landers earthquake. *J. Geophys. Res*, 112:B09411, 2007.

H. Perfettini and J.-P. Ampuero. Dynamics of a velocity strengthening fault region: Implications for slow earthquakes and postseismic slip. *J. Geophys. Res.*, 113:B09411, 2008.

H. Perfettini and J. P. Avouac. Postseismic relaxation driven by brittle creep: A possible mechanism to reconcile geodetic measurements and the decay rate of aftershocks, application to the Chi-Chi earthquake, Taiwai. *J. Geophys. Res.*, 109:B02304, 2004.

A. E. Ragheb, P. J. Clarke, and S. J. Edwards. GPS sidereal filtering: coordinate- and carrier-phase-level strategies. *J. Geod.*, 81:325–335, 2007.

F. Rolandone, J.-M. Nocquet, P. A. Mothes, P. Jarrin, M. Vallée, N. Cubas, S. Hernandez, M. Plain, S. Vaca, and Y. Font. Areas prone to slow slip events impede earthquake rupture propagation and promote afterslip. *Sci. Adv.*, 4(1):eaao6596, 2018.

S. Ruiz, E. Klein, F. del Campos, E. Rivera, P. Poli, M. Métois, C. Vigny, J.-C. Baez, G. Vargas, F. Leyton, R. Madariaga, and L. Fleitout. The seismic sequence of the 16 september 2015 M_w8.3 Illapel, Chile, earthquake. *Seism. Res. Lett.*, 87(4):789–799, 2016.

J. C. Savage, J. L. Svarc, and S.-B. Yu. Postseismic relaxation and aftershocks. *J. Geophys. Res.*, 112:B06406, 2007.

C. Selle and S. Desai. Optimisation of tropospheric delay estimation parameters by comparison of GPS-based precipitable water vapour estimates with microwave radiometer measurments. *IGS workshop, Sydney, Australia*, 2016.

S. W. Smith and M. Wyss. Displacement on the San Andreas fault subsequent to the 1966 Parkfield earthquake. *Bull. Seism. Soc. Am.*, 58(6):1955–1973, 1968.

J. A. Steketee. On Volterra's dislocations in a semi-infinite elastic medium. *Can. J. Phys.*, 36:192–205, 1958.

I. Tsubokawa, Y. Ogawa, and T. Hayashi. Crustal movements before and after the Niigita earthquake. *J. Geod. Soc. Japan*, 10(3-4):165–171, 1964.

C. Vigny, A. Socquet, S. Peyrat, J.-C. Ruegg, M. Métois, R. Madariaga, S. Morvan, M. Lancieri, R. Lacassin, J. Campos, D. Carrizo, M. Bejar-Pizarro, S. Barrientos, R. Armijo, C. Aranda, M.-C. Valderas-Bermejo, I. Ortega, F. Bondoux, S. Baize, H. Lyon-Caen, A. Pavez, J.-P-. Vilotte, M. Bevis, B. Brooks, R. Smalley, H. Parra, J.-C. Baez, M. Blanco, S. Cimbaro, and E. Kendrick. The 2010 M_w8.8 maule megathrust earthquake of central Chile monitored by GPS. *Science*, 332(6036):1417–1421, 2010.

L. Wennerberg and R. V. Sharp. Bulk-friction modeling of afterslip and the modified Omori law. *Tectonophysics*, 277:109–136, 1997.

J. F. Zumberger, M. B. Heflin, D. C. Jefferson, M. M. Watkins, and F. H. Webb. Precise point positioning for the efficient and robust analysis of gps data from large networks. *J. Geophys. Res.*, 102(B3):5005–5017, 1997.

Tables

	Number of detection	Mean onset time	Median onset time
2010 Maule earthquake (M_w8.8)	8/10 (80%)	1.7 ± 1.8 hours	1.3 hours
2015 Illapel earthquake (M_w8.3)	11/17 (65%)	1.3 ± 1.4 hours	0.4 hours
2016 Pedernales earthquake (M_w8.8)	4/26 (15%)	1.8 ± 2.3 hours	0.8 hours
Overall	23/53 (43%)	1.5 ± 1.9 hours	0.7 hours

Table 1: Statistics about the onset time of postseismic surface displacement. The entire dataset is available in Appendix C.

Figures

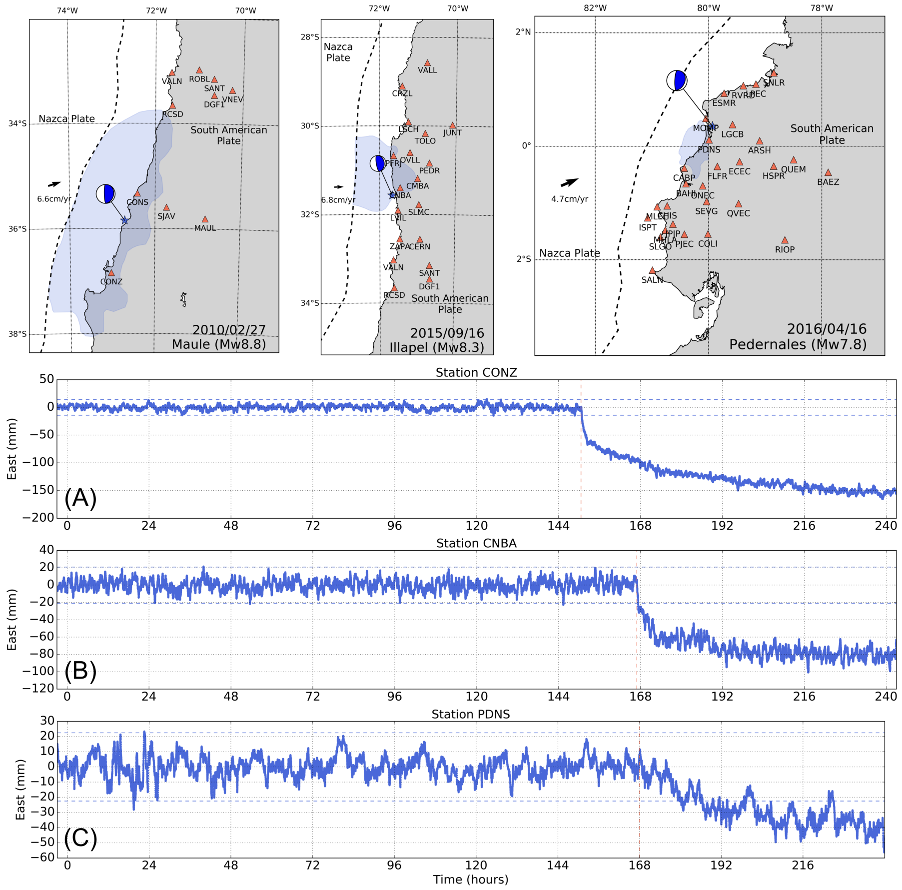

Figure 1: (top row) : Map showing the distribution of continuous GNSS stations for each earthquake considered in this study. There are 10, 17, and 26 stations for the Maule, Illapel, and Pedernales earthquakes, respectively. The continuous GNSS stations for the Maule and Illapel earthquakes are part of the International GNSS Service (IGS) and the Chilean-French International Laboratory (LIA) network. The stations for the Pedernales earthquake are part of the IGEPN (Instituto Geofísico) and IRD (Institut de Recherche pour le Développement) network. The hypocenters (blue stars) are retrieved from the Global Centroid Moment Tensor catalog (http://www.globalcmt.org, last accessed on). The blue shaded areas show the areas of coseismic slip for each earthquake, as inferred by Ruiz et al. (2016), Vigny et al. (2010) and Nocquet et al. (2016). (A) East position time series for the station CONZ for the 2010 Maule, earthquake. (B) East position time series for the station CNBA for the 2015 Illapel, earthquake. (C) East position time series for the station PDNS for the 2016 Pedernales, earthquake. For the three time series, the red dashed line shows the earthquake origin time and the blue dashed line are showing the mean of the time series before the earthquake plus and minus 3.3 times the standard deviation of the time series, also calculated before the earthquake.

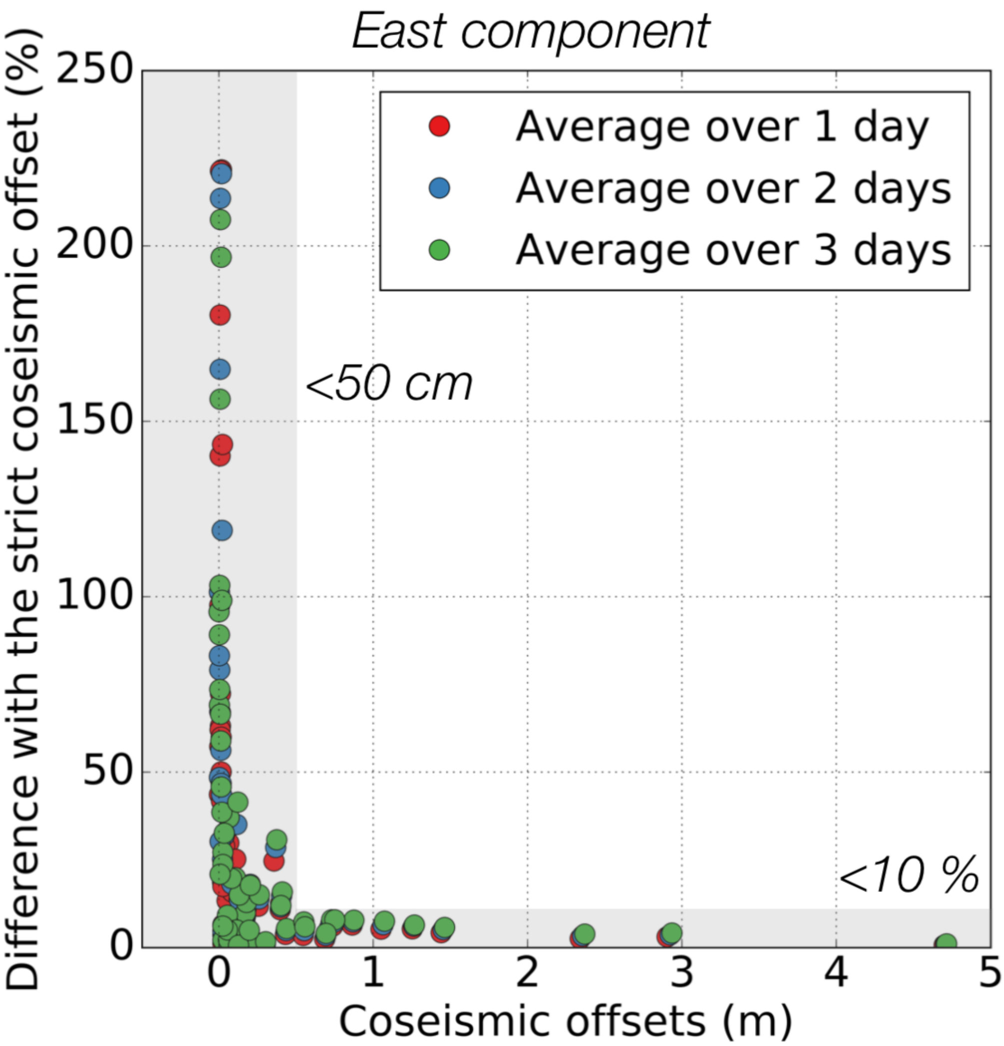

Figure 2: Strict coseismic offsets estimation versus offsets determined using an average of the position time series over 24 hours (red dots), 48 hours (blue dots) and 72 hours (green dots). The horizontal shaded area shows the region where the different estimates do not differ by more than 10%. The vertical shaded area shows the region where the estimates differ by more than 10%, and which is when the measured offsets are less than 50 cm. The dataset used for this Figure is available in Appendix D

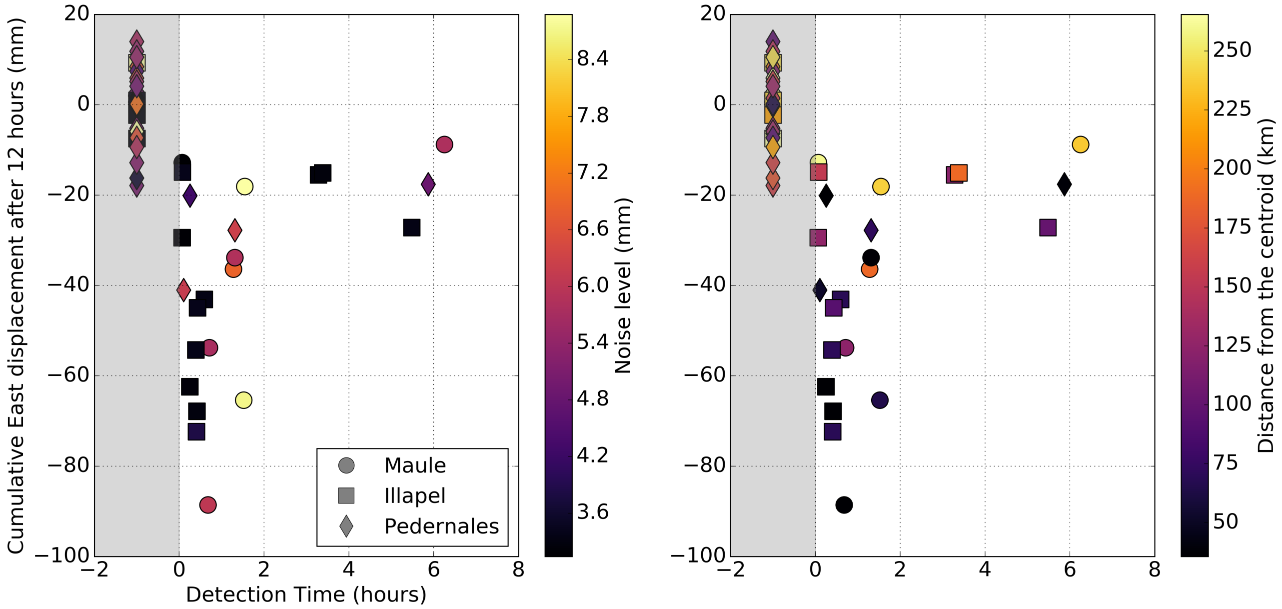

Figure 3: Diagram showing the onset time of the postseismic displacement versus the amplitude of the postseismic displacement measured 12 hours after the earthquake, on the East component. Each point is color-coded with respect to the noise level of the time series on the left side (i.e., the standard deviation of the time series calculated over the 6 days before the earthquake), and with respect to the distance from the centroid on the right side. The onset of postseismic displacement could be detected for 23 stations out of 53 analysed time series (see Table 1). The shape of the symbols corresponds to a given earthquake (see the lower right inset). All the stations that failed the detection test are shown inside the grey area at a fake detection time (-1 hour). The data used to produce this figure are shown in Appendix C.

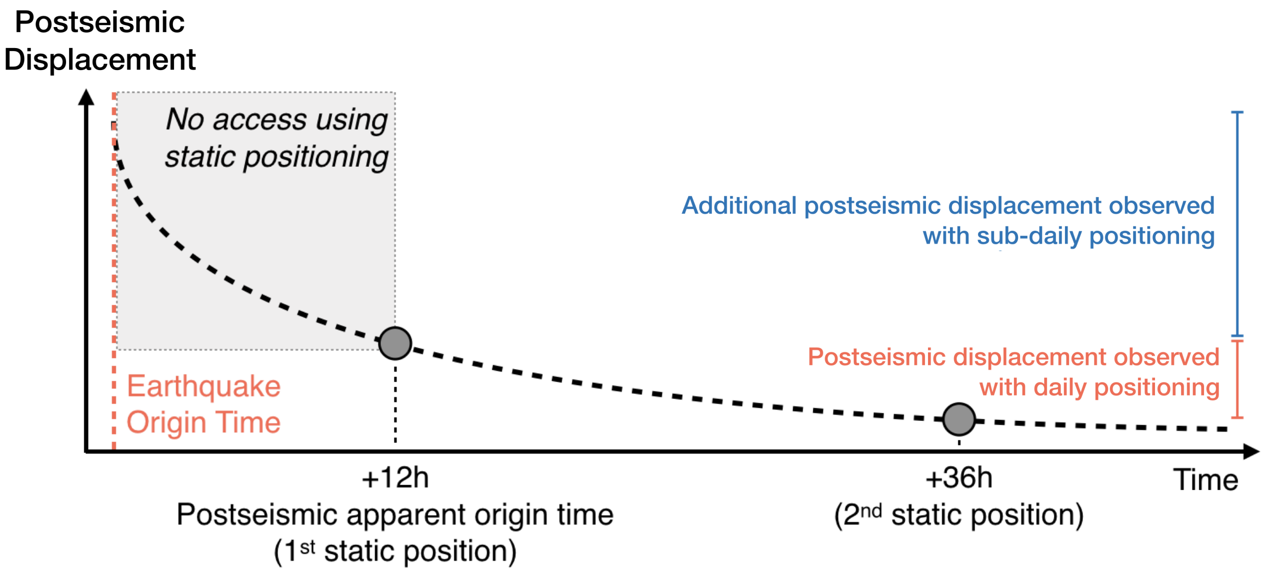

Figure 4: Schematic of the method used to assess the amount of postseismic deformation missed when daily positioning is used. The dashed line shows an idealised decaying postseismic trend. Standard postseismic observations start at the first daily solution, which can be seen as the postseismic apparent origin time. The deformation from the earthquake origin time up to the first daily position can only be resolved using sub-daily position time series.

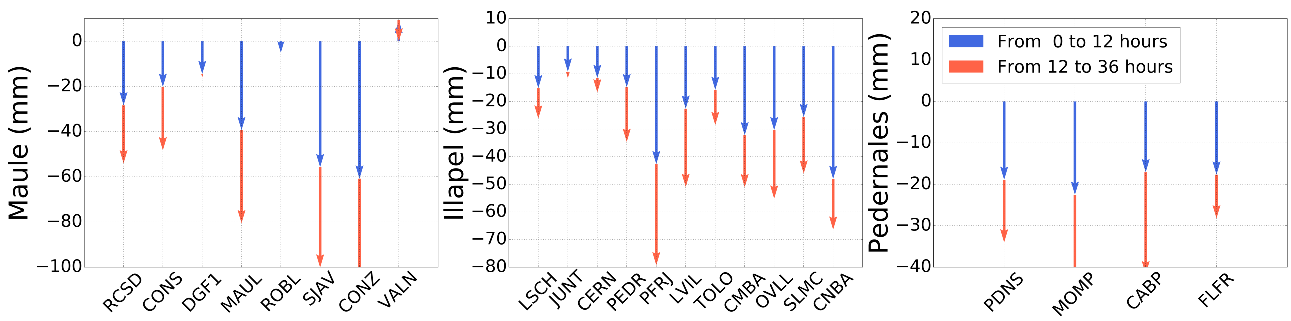

Figure 5: Comparision of the cumulative East displacement observed from 0 to 12 hours (blue arrows) and from 12 to 36 hours (red arrows). Note that the red arrows start at the tip of the blue arrows. Thus, the sum of the two represents the cumulative East displacement over the first 36 hours.

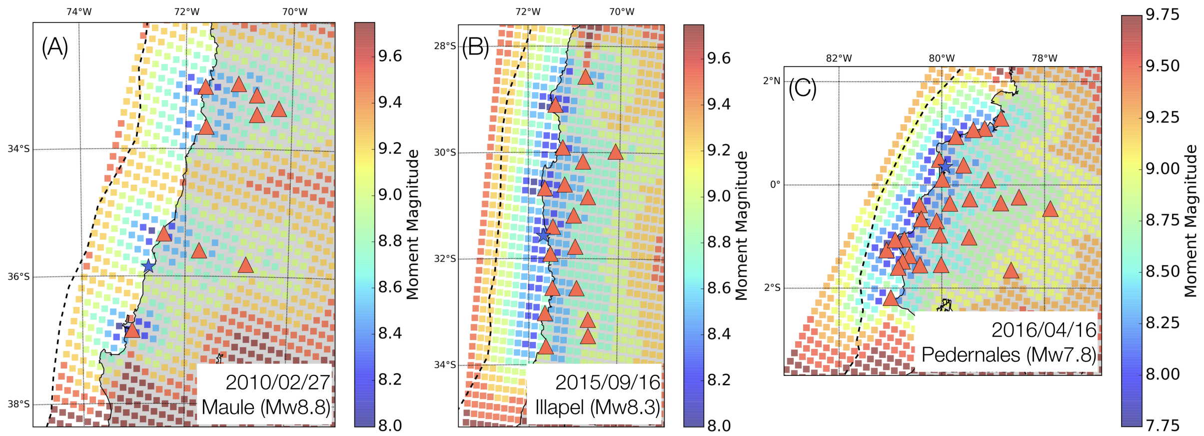

Figure 6: Moment magnitude of the afterslip that can be detected by the network based on the detection procedure used in this study (see the Method Section). The blue star shows the location of the earthquake epicentre. The red triangles are the GNSS receivers. The continuous black line is the coast while the dashed black line shows the trench. The strike, dip and rake of the fault is that of the focal mechanism given by the GCMT catalog. The calculations are based on the approximation of a semi-infinite elastic half-space (Manshina and Smylie 1971, Steketee 1958).

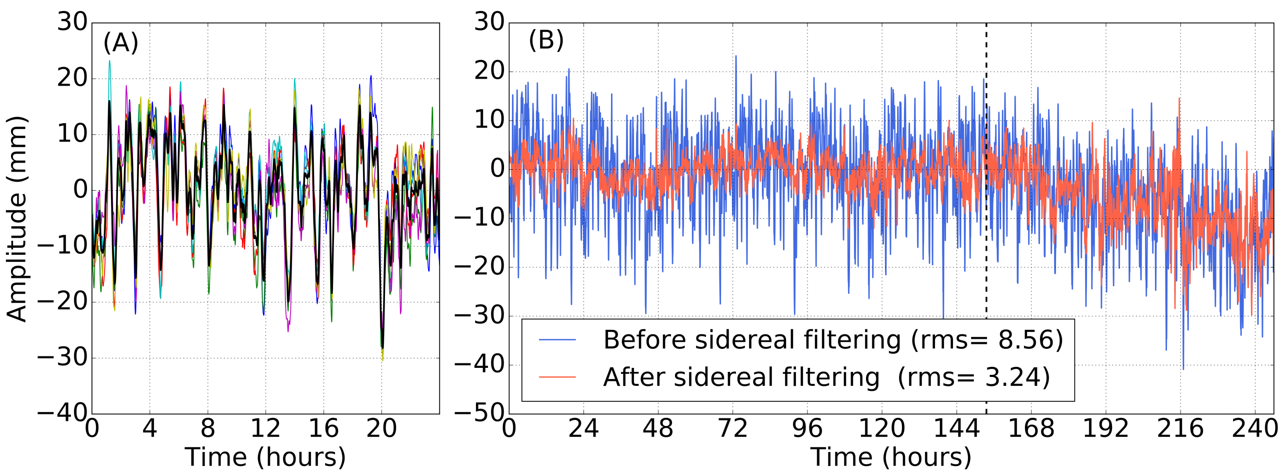

Figure 7: East position time series for station VNEV around the time of the 2010 Maule earthquake (see Figure 1). (A) Sidereal filter. The coloured lines represent the six 24-hours time series preceding the mainshock. The black line is the average of the 6 time series after that they have been properly shifted ans stacked. This is the sidereal filter that is going to be removed from the time series. (B) Position time series before applying the sidereal filter (blue) and after applying the sidereal filter (red). For this specific case, the standard deviation (or RMS) of the time series, calculated using the data before the mainshock, has been reduced from 8.6 mm to 3.5 mm. The vertical dashed line shows the time of the earthquake. Note that the coseismic offset has been removed.

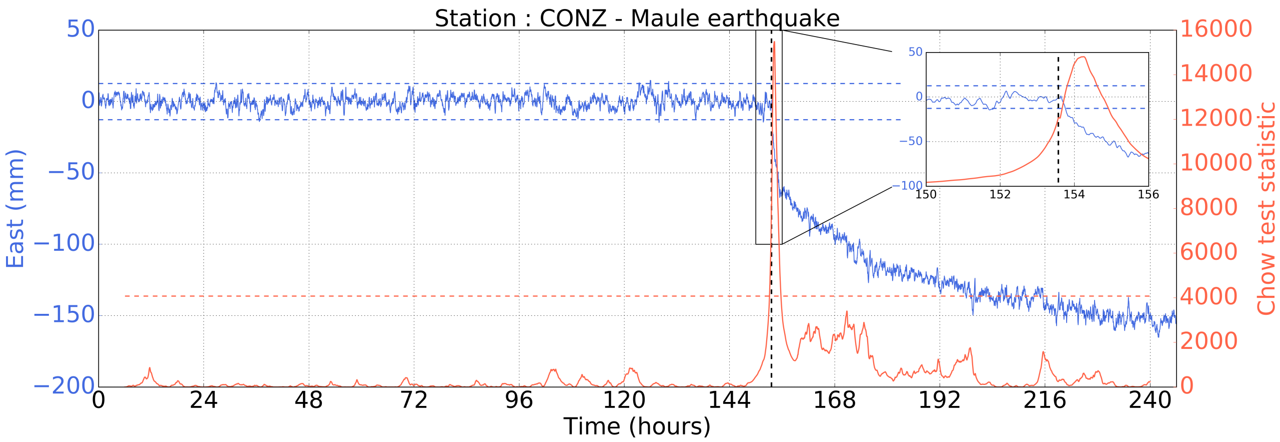

Figure 8: The blue curve shows the East position time series at station CONZ around the time of the 2010 Maule earthquake (see Figure 1). Note that the coseismic offset has been removed from the time series. The blue horizontal dashed lines show the noise level (i.e., the mean of the time series before the earthquake plus and minus 3.3 times the standard deviation of the time series, also calculated from the time series before the earthquake). The vertical dashed line is the earthquake origin time. The red line is the time evolution of the Chow-test statistic (χ) The red horizontal dashed line is the threshold to identify potential ties when significant postseismic deformation might occur. Finally, the detection time is validated if the peak is located after the earthquake origin time and it more than 70% of the time series after the peak remains outside the noise level. For instance, on this figure, significant postseismic deformation is detected ∼41 minutes after the earthquake.

Appendices

A Kinematic precise point positioning strategy

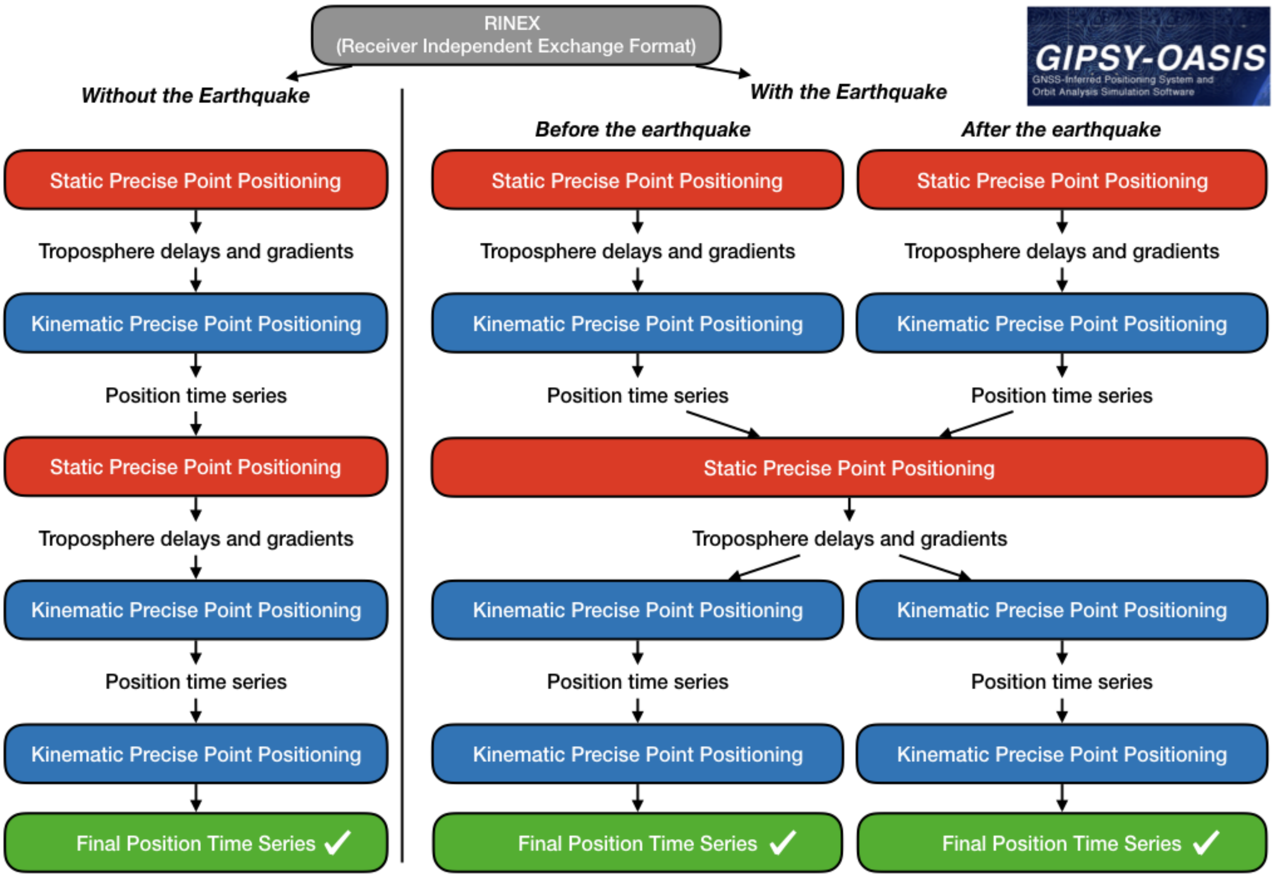

Figure A.1: Schematic that illustrates the processing strategy of the GNSS data. The strategy is mostly based on Malservisi et al. (2015). Note that the processing is different if the RINEX file contains or not the earthquake. Regarding the different parameters of the processing: (1) the static runs are done at a sampling rate of 300 seconds while the kinematic runs are done at a sampling rate of 30 seconds. (2) We use a satellite cutoff angle of 7°. (3) Each satellite must be locked for at least 20 minutes to be considered during the processing. (4) All other parameters are set up as recommended by the JPL documentation. Figure A.2 shows a pseudo-code of the processing routine.

```
> teqc -O.obs L1L2C1C2P1P2 -O.s G -R -O.st YYYY mm (DD-1) 21 00 00.00 -O.e YYYY mm (DD+1) 03 00 00.00 RINEX.LIST > RINEX.NEW
> clockprep -i RINEX.NEW -o RINEX.PREP -fixonlyphase -nocopy
> tropnominal -n XXXX -m VMF1GRID -latdeg 00.00 -londeg 00.00 -h_m 00.00 -stsec 00.00 -endsec 00.00 -samp 300
> cat XXXX.TDPdry XXXX.TDPwet > XXXX.TDPdryandwet
> antex2xyz -antexfile igs14_1958.atx -xyzfile XXXX_antex.xyz -anttype XX -recname XXXX -radcode XX -fel 0 -del 5 -daz 5 -extrap

> (gd2p.pl -i RINEX.PREP -n XXXX -d YYYY-mm-DD -r 300 -type s -w_elmin 7 -eldepwght SQRTSIN
    -e "-a 20 -PC -LC -F -t1 TSTART -t2 TSTOP" -pb_min_slip 1.0E-3 -pb_min_elev 30 -amb_res 2 -dwght 1.0E-5 1.0E-3
    -post_wind 5.0E-3 5.0E-5 -trop_z_rw 9.0E-8 -wetzgrad 5.0E-9 -trop_map VMF1GRID -tdp_in XXXX.TDPdryandwet
    -tides WahrK1 FreqDepLove OctTid PolTid -add_ocnld " -c FES2004.COEFF" -OcnldCpn -add_ocnldpoltid  -ion_2nd
    -shell_height 600 -tec_mdl iri -orb_clk "flinnR /JPLORBCLK" -AntCal XXXX_antex.xyz
    -p 1234.56789 1234.56789 1234.56789 -env_km 0.0 0.0 0.00001234 -stacov > gd2p.log ) >& gd2p.err
```

!! In case of an earthquake, run two times: One time up to 30s before the earthquake and one time 150s after the earthquake !!

```
> grep -P 'TRP|WETZ' tdp_final > XXXX_STATIC.TDPwetanddry ; cat XXXX.TDPdry >> XXXX_STATIC.TDPwetanddry

> (gd2p.pl -i RINEX.PREP -n XXXX -d YYYY-mm-DD -r 30 -type k -w_elmin 7 -eldepwght SQRTSIN
    -e "-a 20 -PC -LC -F -t1 TSTART -t2 TSTOP" -pb_min_slip 1.0E-3 -pb_min_elev 30 -amb_res 2 -dwght 1.0E-5 1.0E-3
    -post_wind 5.0E-3 5.0E-5 -trop_z_rw 9.0E-8 -wetzgrad 5.0E-9 -trop_map VMF1GRID -tdp_in XXXX_STATIC.TDPwetanddry
    -tides WahrK1 FreqDepLove OctTid PolTid -add_ocnld " -c FES2004.COEFF" -OcnldCpn -add_ocnldpoltid -ion_2nd
    -shell_height 600 -tec_mdl iri -orb_clk "flinnR /JPLORBCLK" -AntCal XXXX_antex.xyz
    -p 1234.56789 1234.56789 1234.56789 -env_km 0.0 0.0 0.00001234 -stacov
    -kin_sta_xyz 1.0E-3 3.0E-7 30 RANDOMWALK > gd2p.log ) >& gd2p.err
```

!! In case of an earthquake, run two times: One time up to 30s before the earthquake and one time 150s after the earthquake !!

!! if no earthquake:

```
    > grep 'STA [XYZ]' tdp_final > XXXX_KINE.TDPstawetanddry ; cat XXXX.TDPdryandwet >> XXXX_KINE.TDPstawetanddry
```

!! if earthquake:

```
    > grep 'STA [XYZ]' tdp_final_before >    XXXX_KINE.TDPstawetanddry
    > grep 'STA [XYZ]' tdp_final_after   >> XXXX_KINE.TDPstawetanddry
    > cat XXXX.TDPdryandwet              >> XXXX_KINE.TDPstawetanddry

> (gd2p.pl -i RINEX.PREP -n XXXX -d YYYY-mm-DD -r 300 -type s -w_elmin 7 -eldepwght SQRTSIN
    -e "-a 20 -PC -LC -F -t1 TSTART -t2 TSTOP" -pb_min_slip 1.0E-3 -pb_min_elev 30 -amb_res 2 -dwght 1.0E-5 1.0E-3
    -post_wind 5.0E-3 5.0E-5 -trop_z_rw 9.0E-8 -wetzgrad 5.0E-9 -trop_map VMF1GRID -tdp_in XXXX_KINE.TDPstawetandry
    -tides WahrK1 FreqDepLove OctTid PolTid -add_ocnld " -c FES2004.COEFF" -OcnldCpn -add_ocnldpoltid -ion_2nd
    -shell_height 600 -tec_mdl iri -orb_clk "flinnR /JPLORBCLK" -AntCal XXXX_antex.xyz
    -p 1234.56789 1234.56789 1234.56789 -env_km 0.0 0.0 0.00001234 -stacov > gd2p.log ) >& gd2p.err

> grep -P 'TRP|WETZ' tdp_final > XXXX_STATIC.TDPwetanddry ; cat XXXX.TDPdry >> XXXX_STATIC.TDPwetanddry

> (gd2p.pl -i RINEX.PREP -n XXXX -d YYYY-mm-DD -r 30 -type k -w_elmin 7 -eldepwght SQRTSIN
    -e "-a 20 -PC -LC -F -t1 TSTART -t2 TSTOP" -pb_min_slip 1.0E-3 -pb_min_elev 30 -amb_res 2 -dwght 1.0E-5 1.0E-3
    -post_wind 5.0E-3 5.0E-5 -trop_z_rw 9.0E-8 -wetzgrad 5.0E-9 -trop_map VMF1GRID -tdp_in XXXX_STATIC.TDPwetanddry
    -tides WahrK1 FreqDepLove OctTid PolTid -add_ocnld " -c FES2004.COEFF" -OcnldCpn -add_ocnldpoltid
    -ion_2nd -shell_height 600 -tec_mdl iri -orb_clk "flinnR /JPLORBCLK" -AntCal XXXX_antex.xyz
    -p 1234.56789 1234.56789 1234.56789 -env_km 0.0 0.0 0.00001234 -stacov
    -kin_sta_xyz 1.0E-3 3.0E-7 30 RANDOMWALK > gd2p.log ) >& gd2p.err
```

!! In case of an earthquake, run two times: One time up to 30s before the earthquake and one time 150s after the earthquake !!

```
> cp XXXX_STATIC.TDPdryandwet XXXX_KINE_STATIC.TDPstawetanddry
> grep 'STA [XYZ]' tdp_final >> XXXX_KINE_STATIC.TDPstawetanddry

> (gd2p.pl -i RINEX.PREP -n XXXX -d YYYY-mm-DD -r 30 -type k -w_elmin 7 -eldepwght SQRTSIN
    -e "-a 20 -PC -LC -F -t1 TSTART -t2 TSTOP" -pb_min_slip 1.0E-3 -pb_min_elev 30 -amb_res 2 -dwght 1.0E-5 1.0E-3
    -post_wind 5.0E-3 5.0E-5 -trop_z_rw 9.0E-8 -wetzgrad 5.0E-9 -trop_map VMF1GRID -tdp_in XXXX_KINE_STATIC.TDPstawetanddry
    -tides WahrK1 FreqDepLove OctTid PolTid -add_ocnld " -c FES2004.COEFF" -OcnldCpn -add_ocnldpoltid
    -ion_2nd -shell_height 600 -tec_mdl iri -orb_clk "flinnR /JPLORBCLK" -AntCal XXXX_antex.xyz
    -p 1234.56789 1234.56789 1234.56789 -env_km 0.0 0.0 0.00001234 -stacov
    -kin_sta_xyz 1.0E-3 3.0E-7 30 RANDOMWALK > gd2p.log ) >& gd2p.err
```

!! In case of an earthquake, run two times: One time up to 30s before the earthquake and one time 150s after the earthquake !!

Figure A.2: Pseudo-code of the processing routine

B Effectiveness of the sidereal filter

The next three figures show the RMS of the time series before and after applying the sidereal filter on all stations in this study. The RMS is the standard deviation of the time series using the positions prior to the earthquake origin time. We show that the effect of the sidereal filter for all stations but we only apply it when the cross-correlation measured during the construction of the filter is greater than 0.3 (see the Method Section). Stations for which the sidereal filter is applied are highlighted by a red square.

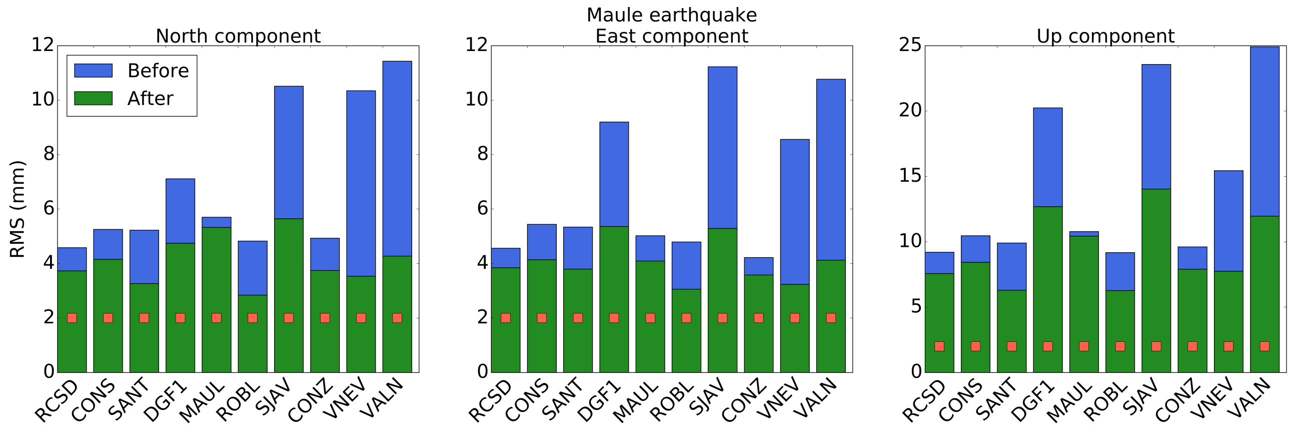

Figure B.1: Quantification of the noise reduction after applying the sidereal filter on each component of each station for the 2010 Maule, Chile, earthquake. The blue bars show the noise level before applying the sidereal filter and the green bars after applying the sidereal filter. The red squares highlight the stations for which we apply the sidereal filter. On average, the RMS is reduced by 38% on the North component, 34% on the East component, and 31% on the Up component.

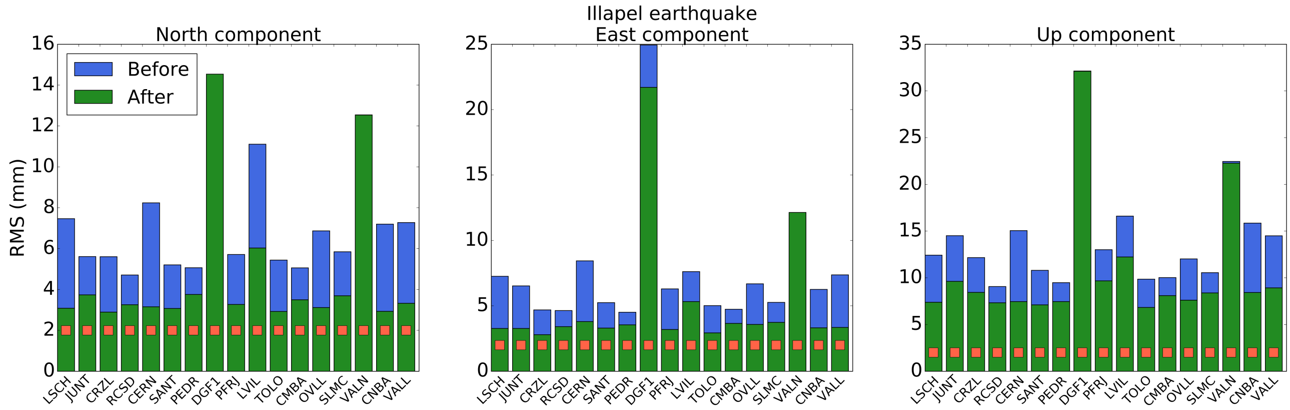

Figure B.2: Quantification of the noise reduction after applying the sidereal filter on each component of each station for the 2015 Illapel, Chile, earthquake. The blue bars show the noise level before applying the sidereal filter and the green bars after applying the sidereal filter. The red squares highlight the stations for which we apply the sidereal filter. On average, the RMS is reduced by 40% on the North component, 32% on the East component, and 27% on the Up component.

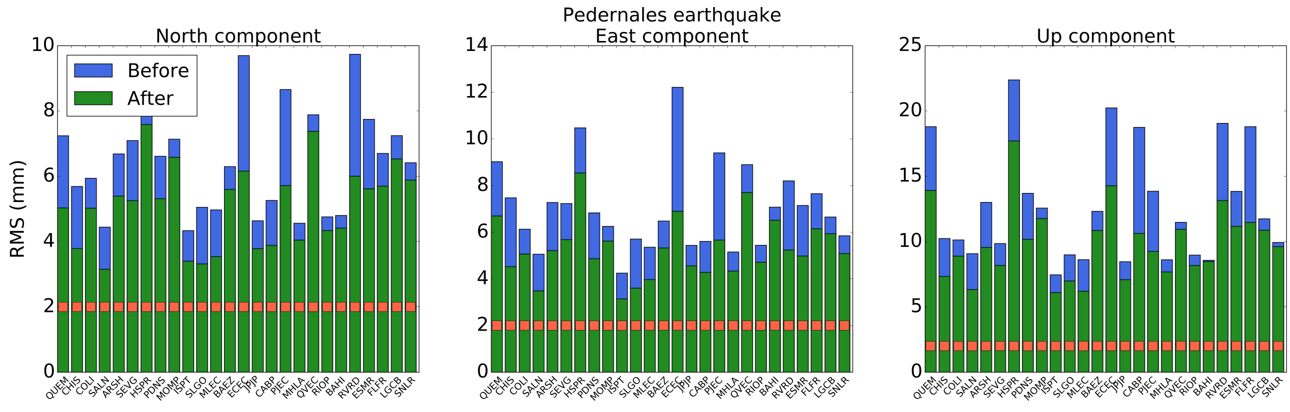

Figure B.3: Quantification of the noise reduction after applying the sidereal filter on each component of each station for the 2016 Pedernales, Ecuador, earthquake. The blue bars show the noise level before applying the sidereal filter and the green bars after applying the sidereal filter. The red squares highlight the stations for which we apply the sidereal filter. On average, the RMS is reduced by 22% on the North component, 10% on the East component, and 18% on the Up component.

C Detection of the onset time

Earthquake name	Station name	Detection Time (hours)	Amplitude at 12 hours (mm)	Noise level (mm)	Distance to the centroid (km)
MAULE	RCSD	1.280	-36.381	4.557	294.174
MAULE	CONS	1.313	-33.830	4.141	98.246
MAULE	SANT	-1.000	2.008	3.798	388.078
MAULE	DGF1	1.547	-18.096	5.358	361.090
MAULE	MAUL	0.713	-53.778	4.096	210.600
MAULE	ROBL	0.072	-12.805	3.061	387.060
MAULE	SJAV	1.522	-65.386	5.291	134.818
MAULE	CONZ	0.680	-88.582	4.223	96.690
MAULE	VNEV	-1.000	0.615	3.235	394.515
MAULE	VALN	6.255	-8.791	4.126	356.389
ILLAPEL	LSCH	3.283	-15.504	3.277	158.091
ILLAPEL	JUNT	3.383	-15.077	3.275	230.198
ILLAPEL	CRZL	-1.000	0.044	2.801	234.841
ILLAPEL	RCSD	-1.000	1.002	3.411	284.244
ILLAPEL	CERN	0.074	-14.883	3.806	192.986
ILLAPEL	SANT	-1.000	-2.261	3.302	261.483
ILLAPEL	PEDR	5.483	-27.163	3.559	137.406
ILLAPEL	DGF1	-1.000	9.302	24.296	291.523
ILLAPEL	PFRJ	0.249	-62.375	3.197	66.659
ILLAPEL	LVIL	0.408	-72.341	5.332	102.422
ILLAPEL	TOLO	0.066	-29.404	2.944	162.734
ILLAPEL	CMBA	0.391	-54.267	3.667	104.016
ILLAPEL	OVLL	0.591	-43.068	3.584	102.844
ILLAPEL	SLMC	0.433	-44.927	3.745	128.873
ILLAPEL	VALN	-1.000	-134.281	11.615	215.349
ILLAPEL	CNBA	0.416	-67.826	3.324	67.069
ILLAPEL	VALL	-1.000	-7.456	3.358	311.841
PEDERNALES	QUEM	-1.000	8.423	6.695	195.319
PEDERNALES	CHIS	-1.000	7.447	4.524	116.593
PEDERNALES	COLI	-1.000	-17.876	5.065	161.012
PEDERNALES	SALN	-1.000	10.545	3.486	244.066
PEDERNALES	ARSH	-1.000	-5.192	5.207	130.314
PEDERNALES	SEVG	-1.000	13.998	5.680	97.931
PEDERNALES	HSPR	-1.000	23.306	8.545	157.762
PEDERNALES	PDNS	5.873	-17.594	4.864	38.621
PEDERNALES	MOMP	1.315	-27.777	6.255	71.725
PEDERNALES	ISPT	-1.000	1.466	3.141	156.568
PEDERNALES	SLGO	-1.000	-16.213	3.606	177.539
PEDERNALES	MLEC	-1.000	-0.205	3.969	128.016
PEDERNALES	BAEZ	-1.000	5.920	6.455	265.492
PEDERNALES	ECEC	-1.000	49.985	6.898	90.339
PEDERNALES	JPJP	-1.000	11.835	5.436	145.481
PEDERNALES	CABP	0.256	-20.113	4.279	35.676
PEDERNALES	PJEC	-1.000	5.142	5.665	160.462
PEDERNALES	MHLA	-1.000	-6.337	4.339	161.709
PEDERNALES	QVEC	-1.000	-5.908	8.879	131.808
PEDERNALES	RIOP	-1.000	10.549	5.440	246.101
PEDERNALES	BAHI	-1.000	0.169	7.070	62.140
PEDERNALES	RVRD	-1.000	-12.804	5.238	163.365
PEDERNALES	ESMR	-1.000	4.118	4.981	131.028
PEDERNALES	FLFR	0.106	-41.018	6.146	52.424
PEDERNALES	LGCB	-1.000	-7.288	6.633	93.513
PEDERNALES	SNLR	-1.000	-9.349	5.846	221.367

Table C.3: Details about the data used to produce Figure 3 and Table 1 in the main text. Note that the detection procedure is only applied on the East component. Note that when the detection time is -1, it means that no significant postseismic signal has been detected.

D Error on the coseismic offsets

The table below summarises the data used to produce Figure 2 in the main text. Note that the calculations are made only for the East component. In brackets, we show the percentage of difference with respect to the strict coseismic offsets. The term 1 day, 2 days and 3 days are the different time windows that we use to compute the average position on either side to the earthquakes origin time.

Maule earthquake:				
Station name	strict offsets (mm)	1 day offsets (mm)	2 days offsets (mm)	3 days offsets (mm)
RCSD	-676.4003	-713.4804 (5.48)	-723.8694 (7.02)	-730.0030 (7.92)
CONS	-4663.2833	-4697.7939 (0.74)	-4707.8679 (0.96)	-4715.1020 (1.11)
SANT	-248.5500	-248.0187 (0.21)	-250.7926 (0.90)	-251.9147 (1.35)
DGF1	-413.0500	-428.5607 (3.76)	-433.4208 (4.93)	-435.6112 (5.46)
MAUL	-996.3750	-1048.9133 (5.27)	-1062.3350 (6.62)	-1072.2166 (7.61)
ROBL	-154.6400	-166.5790 (7.72)	-169.2466 (9.45)	-170.0421 (9.96)
SJAV	-2279.6000	-2338.8814 (2.60)	-2356.7265 (3.38)	-2368.3783 (3.89)
CONZ	-2817.4000	-2903.8465 (3.07)	-2922.7570 (3.74)	-2934.7930 (4.17)
VNEV	-295.6667	-296.9626 (0.44)	-298.7592 (1.05)	-300.8467 (1.75)
VALN	-87.2333	-101.6065 (16.48)	-103.2041 (18.31)	-104.6905 (20.01)
Illapel earthquake:				
Station name	strict offsets (mm)	1 day offsets (mm)	2 days offsets (mm)	3 days offsets (mm)
LSCH	-156.8571	-171.0205 (9.03)	-174.7044 (11.38)	-177.1400 (12.93)
JUNT	-113.1571	-128.5675 (13.62)	-128.7922 (13.82)	-130.0923 (14.97)
CRZL	-23.1000	-22.8193 (1.22)	-23.9411 (3.64)	-23.5998 (2.16)
RCSD	-2.4143	-1.3604 (43.65)	-1.2431 (48.51)	-0.1024 (95.76)
CERN	-47.4571	-61.6560 (29.92)	-63.7426 (34.32)	-65.0911 (37.16)
SANT	-18.0143	-21.3808 (18.69)	-22.5605 (25.24)	-22.9200 (27.23)
PEDR	-510.7000	-538.7434 (5.49)	-544.9800 (6.71)	-548.5015 (7.40)
DGF1	-14.1667	5.6892 (140.16)	-2.9523 (79.16)	-1.5298 (89.20)
PFRJ	-1380.5571	-1439.1194 (4.24)	-1452.3871 (5.20)	-1460.9975 (5.83)
LVIL	-285.0857	-355.5782 (24.73)	-366.5318 (28.57)	-372.9432 (30.82)
TOLO	-226.9143	-253.8072 (11.85)	-258.5451 (13.94)	-261.2538 (15.13)
CMBA	-809.8991	-862.3400 (6.47)	-869.6235 (7.37)	-873.7081 (7.88)
OVLL	-693.3714	-735.9753 (6.14)	-743.7877 (7.27)	-748.6480 (7.97)
SLMC	-352.9571	-397.6396 (12.66)	-405.1986 (14.80)	-408.9895 (15.88)
VALN	106.9017	2.4730 (97.69)	-1.5320 (101.43)	-3.5481 (103.32)
CNBA	-1187.5429	-1251.7268 (5.40)	-1260.4030 (6.14)	-1264.1526 (6.45)
VALL	-4.5333	-14.5864 (221.76)	-14.5344 (220.61)	-13.4591 (196.89)
Pedernales earthquake:				
Station name	strict offsets (mm)	1 day offsets (mm)	2 days offsets (mm)	3 days offsets (mm)
QUEM	-59.2500	-51.2707 (13.47)	-54.1553 (8.60)	-53.7952 (9.21)
CHIS	-27.2286	-15.8598 (41.75)	-15.3256 (43.72)	-16.7118 (38.62)
COLI	7.5001	-9.1112 (221.48)	-8.5194 (213.59)	-8.0671 (207.56)
SALN	-23.6571	-11.7961 (50.14)	-10.3532 (56.24)	-9.7174 (58.92)
ARSH	-105.4000	-108.7341 (3.16)	-109.9424 (4.31)	-110.7700 (5.09)
SEVG	-48.0857	-34.1320 (29.02)	-32.6949 (32.01)	-32.3760 (32.67)
HSPR	-99.6286	-83.7463 (15.94)	-81.5415 (18.15)	-79.8990 (19.80)
PDNS	-666.5013	-682.9228 (2.46)	-689.6675 (3.48)	-693.7728 (4.09)
MOMP	-84.8143	-106.2321 (25.25)	-114.6005 (35.12)	-120.0085 (41.50)
ISPT	-6.5857	-2.8066 (57.38)	-1.1038 (83.24)	-2.0310 (69.16)
SLGO	8.3429	-6.7067 (180.39)	-5.4153 (164.91)	-4.7036 (156.38)
MLEC	-59.4571	-60.1958 (1.24)	-59.4273 (0.05)	-60.8047 (2.27)
BAEZ	-30.1143	-24.8603 (17.45)	-23.6291 (21.54)	-22.9700 (23.72)
ECEC	-246.5429	-206.0553 (16.42)	-201.8984 (18.11)	-202.7029 (17.78)
JPJP	-23.3143	-8.5671 (63.25)	-7.6650 (67.12)	-7.7974 (66.56)
CABP	-525.1429	-543.3145 (3.46)	-550.6044 (4.85)	-556.3711 (5.95)
PJEC	-13.5286	-5.1175 (62.17)	-4.4238 (67.30)	-3.5603 (73.68)
MHLA	-4.6286	-7.9820 (72.45)	-6.0295 (30.27)	-5.5969 (20.92)
QVEC	-51.2993	-54.4295 (6.10)	-54.3216 (5.89)	-53.9211 (5.11)
BAHI	-123.7003	-123.1828 (0.42)	-124.0904 (0.32)	-124.5988 (0.73)
RVRD	-8.4000	-20.4554 (143.52)	-18.3902 (118.93)	-16.7223 (99.08)
ESMR	-25.3005	-23.6292 (6.61)	-24.0841 (4.81)	-23.7315 (6.20)
FLFR	-356.2286	-394.9591 (10.87)	-397.5719 (11.61)	-399.1921 (12.06)
LGCB	-185.0993	-189.8746 (2.58)	-193.1560 (4.35)	-194.2354 (4.94)
SNLR	-8.4000	-13.4473 (60.09)	-12.3391 (46.89)	-12.2502 (45.84)

Table D.3: Details of the values used to produce Figure 2 in the main text.